

Article

One-Pot Hydrothermal Synthesis of Novel Cu-MnS with PVP Cabbage-Like Nanostructures for High-Performance Supercapacitors

S. Srinivasa Rao ¹, Ikkurthi Kanaka Durga ², Bandari Naresh ², Bak Jin-Soo ², T.N.V. Krishna ², Cho In-Ho ², Jin-Woo Ahn ¹ and Hee-Je Kim ^{2,*}

¹ Department of Mechatronics Engineering, Kyungsoong University, 309 Suyeong-ro, Nam-gu, Busan 48434, Korea; srinu.krs@gmail.com (S.S.R.); jwahn@ks.ac.kr (J.-W.A.)

² School of Electrical Engineering, Pusan National University, Busandaehak-ro 63beon-gil, Geumjeong-gu, Busan 46241, Korea; kanakadurga.ikkurthi@gmail.com (I.K.D.); naresh1.bandari@gmail.com (B.N.); imjsn17@pusan.ac.kr (B.-J.S.); vamsik.tirumalasetty@gmail.com (T.N.V.K.); whdlsgh92@icloud.com (C.I.-H.)

* Correspondence: heeje@pusan.ac.kr; Tel.: +82-51-510-2364; Fax: +82-51-513-0212

Received: 28 April 2018; Accepted: 13 June 2018; Published: 17 June 2018



Abstract: This paper reports the facile synthesis of a novel architecture of Cu-MnS with PVP, where the high theoretical capacitance of MnS, low-cost, and high electrical conductivity of Cu, as well as appreciable surface area with high thermal and mechanical conductivity of PVP, as a single entity to fabricate a high-performance electrode for supercapacitor. Benefiting from their unique structures, the Cu-MnS with 2PVP electrode materials show a high specific capacitance of 833.58 F g^{-1} at 1 A g^{-1} , reversibility for the charge/discharge process, which are much higher than that of the MnS-7 h, Cu-MnS, and Cu-MnS with 1 and 3PVP. The presence of an appropriate amount of PVP in Cu-MnS is favorable for improving the electrochemical performance of the electrode and the existence of Cu was inclined to enhance the electrical conductivity. The Cu-MnS with 2PVP electrode is a good reference for researchers to design and fabricate new electrode materials with enhanced capacitive performance.

Keywords: supercapacitors; cabbage plant like nanostructured; Cu-MnS with PVP; electrochemical studies; stability

1. Introduction

Research related to energy production, storage, and distribution is becoming increasingly important due to the large proliferation of portable electronics, auxiliary power sources, and hybrid electric vehicles in recent years [1,2]. The two most frequently used energy storage devices are lithium ion batteries and electrolytic capacitors. Lithium ion batteries have a very low power density with low cycle life and suffering from ageing and it can explode due to overcharge [3,4]. In contrast, electrolytic capacitors also can explode due to the spark ignition of free oxygen or high gas pressures and it shows a low energy density [5]. Therefore, both commonly used energy storage devices are not secure and suitable when high energy and power densities are required. From an energy storage perspective, supercapacitors with high power densities of 10 kW kg^{-1} with excellent energy densities of approximately $150\text{--}200 \text{ W h kg}^{-1}$ are the prominent options [6]. Depending on their energy storage mechanism, supercapacitors are categorized mainly into three groups: electric double layer capacitors (EDLC), pseudocapacitors, and hybrid electrochemical capacitors. EDLC consisting of carbon based materials such as carbon nanotubes, carbon hollow nanospheres, activated carbon, graphene, nitrogen-doped carbon nanofibers, and storage charge via the electrostatic interactions of ions at the electrode/electrolyte interface, and thus exhibit relatively low specific capacitance (SC); however, hybrid electrochemical capacitors usually consist of one battery-type Faradaic electrode

with another capacitive electrode in the entire device [7,8]. Pseudocapacitors usually consisting of metal oxide/hydroxide or conducting polymer electrodes display higher energy density and higher specific capacitance, and redox reactions take place at the surface of the electroactive materials. Therefore, pseudocapacitors have attracted considerable research interest in recent years and exhibited a higher SC ($300\text{--}1000\text{ F g}^{-1}$) than that of EDLC [9]. Pseudocapacitors have many other benefits, such as excellent performance and high power density, compared to traditional lithium ion batteries. Therefore, pseudocapacitors are promising devices for low cost, easy to maintain, fast charging, small size, extensive range of setup temperatures, high-performance energy storage, eco-friendly, and safe applications [10,11].

On the other hand, many studies of traditional pseudocapacitor materials have been limited by the lack of high performance with a facile preparation method or reasonable cost. In addition, the electrochemical stability or cycling performance of polymer composite electrodes is challenging with a $>10\%$ reduction of SC after 1000 charging/discharging cycles. Moreover, the high-performance energy storage electronic devices currently used in industry are susceptible to accidental fire damage due to electrolyte leakage, overheating, and current overflow [12,13]. These issues have prevented their wider use by traditional companies manufacturing modern electronic devices. These problems can be resolved and these devices can be made secure by synthesizing hybrid ternary nanocomposites with pseudocapacitor materials.

Transition metal nitrides (TMNs) have been investigated widely for supercapacitor applications. On the other hand, the synthesis of TMNs is a very difficult and time consuming process due to the formation of $\text{N}\equiv\text{N}$ bonds [14]. Moreover, it shows instability in humid atmospheres and air, which can drastically alter the physicochemical properties and turn the energy storage performance of the material. Among the metal sulfides candidates, manganese sulfide (MnS) exhibits intriguing characteristics, such as low-cost, exceptional electrochemical performance, environmental friendliness, and natural abundance [15,16]. This is the most promising electrode material for the next generation supercapacitors because of its high theoretical SC of 1370 F g^{-1} in aqueous electrolytes. Compared to ternary transition metal oxides, metal sulfides often exhibit higher conductivity, ionic diffusivity compared to metal oxides due to the substitution of oxygen with sulfur atoms, narrow band gap, large anionic polarizability, and larger sizes of the S^{2-} ion [15,17]. On the other hand, regardless of its high theoretical SC value, the experimental SC of MnS supercapacitors is much lower than that of the anticipated value owing to its meager electronic conductivity ($10^{-5}\text{--}10^{-6}\text{ S cm}^{-1}$), low surface area of $10\text{--}80\text{ m}^2\text{ g}^{-1}$, and poor cyclic stability. The SC value and electrical conductivity of the MnS electrode material can be enhanced further by synthesizing a binary composite with copper (Cu) and polyvinyl pyrrolidone (PVP). Composite materials possess synergistic improvements in properties, such as cycling stability, charge transfer resistance, and chemical activity to poisoning for SCs, which are greatly superior to a simple combination of individual components [18]. Among the many metallic materials, Cu has attracted significant interest because of its essential roles in metal-catalyzed reactions and its environmental credentials. In addition, Cu is of particular interest because of its high electrical conductivity and it is used widely in catalysts, resins, thermal conduction, and electronics [19].

Mochao Cai et al. reported the PVP-assisted synthesis of a Fe_3O_4 /graphene composite for lithium storage applications [20]. The presence of PVP molecules stabilized the graphene oxide suspension and enhanced the reversible capacity, cycling performance, and rate capability significantly. Furthermore, PVP nanoparticles are the least toxic, have a high surface area, and show fast electron communication features; hence, they have been used extensively as nanosensors for a range of biomolecules and ions. Xumin Zhang et al. used PVP to modify graphene oxide for enhancing the thermal and mechanical conductivity and observed appreciable results [21,22].

This paper reports the facile synthesis of a novel architecture of Cu-MnS with PVP, where the complementary features of high theoretical capacitance of MnS, low-cost, and high electrical conductivity of Cu as well as the appreciable surface area with high thermal and mechanical conductivity of PVP, on a single entity on nickel foam to fabricate a high-performance electrode

for supercapacitor applications. The active phase of Cu and PVP in MnS promotes ion diffusion on the interfaces, and the void space between the particles can endure the volume change in long-term cycling. The electrochemical tests revealed the as-prepared Cu-MnS with the 2PVP electrode to have an extraordinary SC of 833.58 F g^{-1} at a current density of 1 A g^{-1} and very high cycling stability of 96.95% over 1000 cycles in a 2 M KOH solution. Therefore, it can provide a new pathway towards the commercialization of Cu-MnS with PVP-based supercapacitors.

2. Experimental Methods

2.1. Materials

Manganese sulfate monohydrate [$\text{MnSO}_4 \cdot \text{H}_2\text{O}$], sodium sulfate [Na_2SO_4], ammonium persulfate [$(\text{NH}_4)_2\text{S}_2\text{O}_8$], copper sulfate pentahydrate [$\text{CuSO}_4 \cdot 5\text{H}_2\text{O}$], polyvinyl pyrrolidone, polyvinylidene fluoride, potassium hydroxide KOH, 1-methyl-2-pyrrolidinone were purchased from Sigma Aldrich. Carbon black acetylene was purchased from Alfa Aesar. All chemicals used in the experiment were of analytical grade and used as received.

2.2. Synthesis of Cu-MnS with PVP Nanoparticles

In a typical synthesis of MnS, 0.1 M $\text{MnSO}_4 \cdot \text{H}_2\text{O}$, 0.1 M Na_2SO_4 , and 0.1 M of $(\text{NH}_4)_2\text{S}_2\text{O}_8$ were dissolved in 30 mL of deionized water with vigorous stirring. The solution was stirred for 30 min under ambient conditions to form a clear white color solution and then transferred to a Teflon lined stainless steel autoclave heated to $150 \text{ }^\circ\text{C}$ for 5 h. After cooling naturally to room temperature, the as-obtained MnS material was collected, filtered, and washed several times with deionized water and ethanol to remove the excess reactants and loosely bound ions. The black precipitates were collected and dried in an oven at $80 \text{ }^\circ\text{C}$ for 10 h to enhance the specific surface area. Cu-doped MnS and Cu-doped MnS with PVP were prepared using the same procedure, where 10 wt. % of $\text{CuSO}_4 \cdot 5\text{H}_2\text{O}$ and/or polyvinyl pyrrolidone (0.1, 0.2, and 0.3 g) were dispersed into the MnS mixture and heated to $150 \text{ }^\circ\text{C}$ for 5 h.

2.3. Preparation of Working Electrode on Nickel Foam Substrate

The nickel foam substrate with rectangular dimensions of $1 \times 1 \text{ cm}^2$ was used as a substrate because of its good electrical conductivity and desirable 3D porous structure. The nickel foam reduces the diffusion resistance of the redox electrolyte and improves the facility of ion transportation [23,24]. Prior to synthesis, the nickel foam substrates were cleaned with acetone and a 3 M HCl solution for 10 min to remove the surface oxide layer. Finally, the nickel foam was washed with ethanol and deionized water by sonication and dried with a hair dryer. The working electrode was prepared by mixing 75 wt.% of active material, 15 wt.% of carbon black acetylene, and 5 wt.% of polyvinylidene fluoride in 2 mL of 1-methyl-2-pyrrolidinone with stirring overnight. The resulting slurry was loaded on the nickel foam and dried overnight in an oven at $60 \text{ }^\circ\text{C}$. The loading densities of the active materials were acquired by measuring the electrode with a microbalance with an accuracy of 0.01 mg and the weight of the active materials was approximately 5 mg cm^{-2} for all electrodes. The loading was measured by calculating the difference between the measured mass of the active materials coated and uncoated on a nickel foam substrate.

2.4. Characterizations

The resulting MnS, Cu-MnS, and Cu-MnS with PVP electrodes were characterized by field emission scanning electron microscopy (FE-SEM; SU-70, Hitachi, Tokyo, Japan). Their compositions and crystalline structures were characterized by energy-dispersive X-ray spectroscopy (EDX) attached to the FE-SE microscope and powder X-ray diffraction (XRD, Rigaku D/MAX 2500PC, Rigaku Corporation, Tokyo, Japan), which were collected from 20 to $80 \text{ }^\circ\text{C}$ in 2θ with a Cu target and a monochromator at 40 kV and 250 mA. X-ray photoelectron spectroscopy (XPS, KBSI, Busan, Korea) was performed to examine the elemental compositions using Al $K\alpha$ X-rays at 240 W.

2.5. Electrochemical Characterization

The electrochemical tests were carried out in a classical three-electrode setup; hierarchical Cu-MnS with PVP/nickel foam architectures were used directly as the working electrode, platinum wire, and Ag/AgCl as a counter electrode and reference electrode. Cyclic voltammetry (CV, SP-150 Biological Science Instrument, Seyssinet-Pariset, France) was performed at room temperature over the voltage range of -0.5 to 0.5 V at different scan rates using a three and two-electrode cell. The galvanostatic charge–discharge (GCD) cycles were measured within a voltage range of 0.4 to -0.5 V at various current densities to evaluate the SC. To evaluate the SC retention, three thousand cycles were performed at a high current density and the GCD curves were derived. The specific capacitance, area capacitance, and the energy and power densities values was calculated for the single electrodes and their respective equations are given in the supporting information in Sections 1–3. Electrochemical impedance spectroscopy (EIS) was observed using a biologic potentiostat/galvanostat/EIS analyzer (Biological Science Instrument, Seyssinet-Pariset, France) by applying frequencies from 100 KHz to 0.1 Hz and an AC voltage of 5 mV at the open circuit potential.

3. Results and Discussion

Figure 1 presents the fabrication process of MnS, Cu-MnS, and Cu-MnS with PVP samples based on the experimental data. Published reports suggest that nanotubes, nanowires, and nanorods are the most common 1D nanostructures and they have attracted considerable attention due to facile strain relaxation during ion intercalation, efficient 1D electron transport and effective electrode-electrolyte contact because of their large surface-to-volume ratio [25,26]. Cu-MnS with PVP was prepared by mixing MnS, Cu, and PVP solution at specific ratios, as described in the experimental section to achieve efficient and stable materials. The cabbage-like nanostructured sample was prepared by a hydrothermal method at 150 °C for 5 h (Figure 1b). The resulting Cu-MnS with 2PVP wet powder (Figure 1c) was cleaned and filtered with DI water and ethanol and annealed further at 80 °C for 10 h. The powder was then coated on nickel foam and used further for electrochemical reactions.

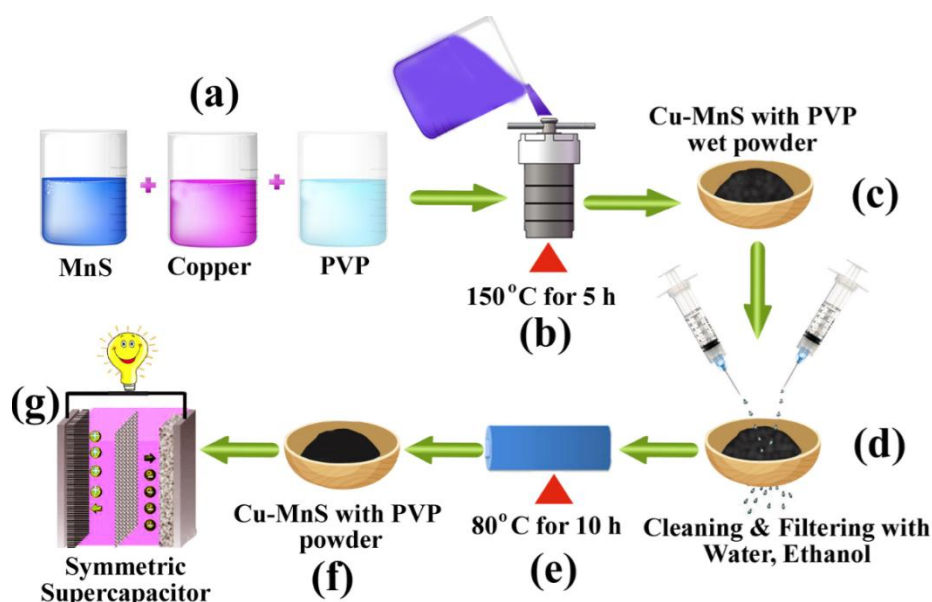


Figure 1. Illustration of the synthesis route for Cu-MnS with PVP nanocomposite.

The crystallographic structure of the product obtained by the hydrothermal method was determined by X-ray power diffraction (XRD). Figure 2a presents the XRD patterns of the MnS-7 h, Cu-MnS, and Cu-MnS with 2PVP nanocomposite. Figure 2a (MnS-7 h) showed broad XRD peaks at

28.53, 34.30, 40.72, 42.61, 56.43, 58.96, 64.79, 67.01, and 72.30° 2 θ . No other characteristic peaks from impurities—such as Mn(OH)₂, MnO, or MnO₂—were detected, which reveals the high-phase purity of the as-prepared MnS. On the other hand, the intensity of the pure MnS peaks decreased gradually with the deposition of Cu and 2PVP in MnS and no XRD peaks were observed for Cu-MnS with 2PVP, indicating that the Cu and PVP were dispersed well in MnS. The observed values are accordance with the reported data (Joint Committee for Powder Diffraction studies file no. 40-1288 and 40-1289).

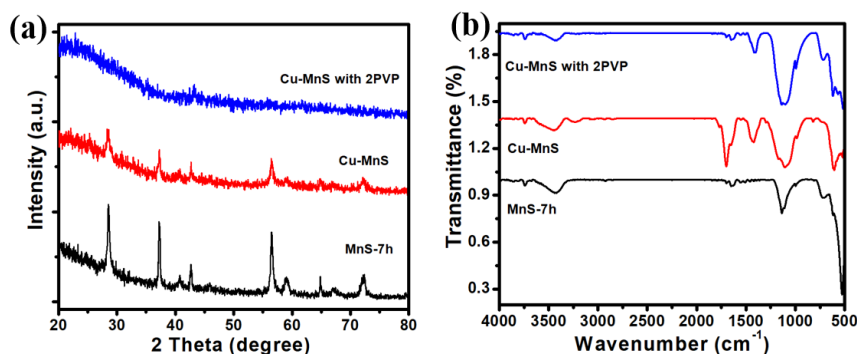


Figure 2. XRD (a) and FTIR (b) patterns of the MnS, Cu-MnS, and Cu-MnS with 2PVP nanocomposite.

The vibrational properties were also studied by Fourier transform infrared (FTIR) spectroscopy, as shown in Figure 2b. The peaks at approximately 646 and 823 cm^{-1} were attributed to the Mn-S stretching vibration and the existence of a resonance interaction between the vibrational modes of sulfide ions in the powder. The additional band observed at approximately 1253 cm^{-1} was assigned to the sulfide source in MnS, indicating the coordination between Mn atoms in MnS. The bands at 3000–3600 cm^{-1} were assigned to the –OH group, indicating the existence of H₂O absorbed in the surface of nanocrystals. The broad absorption peak in the range, 1500–1650 cm^{-1} , were assigned to the C=O stretching modes due to the absorption of carbon dioxide [27,28]. The FTIR spectrum of Cu-MnS and Cu-MnS with 2PVP samples displayed comparable peaks to the spectrum of pure MnS-7 h. The peak at 1253 cm^{-1} was split into multiple peaks, indicating that the doped Cu and PVP affected the structure of MnS.

XPS was conducted to evaluate the chemical states and metal oxidation states of the MnS, Cu-MnS and Cu-MnS with 2PVP materials. Figure 3 shows the corresponding results. All the analysis (XRD, XPS and FTIR spectroscopy) were conducted using the powder to exclude the effects of nickel foam substrate. As shown in Figure 3a, the wide-scan XPS survey spectra of the three different materials confirmed the presence of S2p, C1s, N1s, O1s, Mn2p, and Na1s. The Mn2p spectrum of Cu-MnS with 2PVP nanocomposite could be fitted to two binding energies of 642.00 and 653.85 eV, corresponding to the Mn2p_{3/2} and Mn2p_{1/2}, respectively. The Mn2p for Cu-MnS with the 2PVP nanocomposite showed two strong intensity peaks, which were higher than those of the bare MnS-7 h and Cu-MnS, suggesting the strong formation of Mn in the composite [29]. The presence of Cu and PVP in MnS can increase the electrochemical activity of MnS in the electrochemical process. According to the binding energy separation of Mn2p, a ΔE of 11.85 eV was observed for the resulting materials indicating that the dominant valence of Mn is Mn⁴⁺. Figure 3c presents the S2p spectra of the resulting electrodes; the major peak at 168.1 eV was assigned to the S2p_{3/2} characteristic peak of sulfur in MnS. Copper and PVP were not detected in the Cu-MnS and Cu-MnS with 2PVP due to the low crystallinity and too thin layers of Cu and PVP. The new peak at approximately 163.00 eV in Figure 3c for Cu-MnS with 2PVP can be associated with the partial oxidation of unsaturated S atoms in air. Moreover, from XPS analysis of MnS-7 h, Cu-MnS, and Cu-MnS with 2PVP composites, the presence of Mn (17.97, 9.49, and 2.05%), S (4.22, 9.69, and 6.24% for the MnS, Cu-MnS, and Cu-MnS with 2PVP), O, and C was quite evident without impurities. The XPS curves showed that Mn and S were distributed uniformly and there was a high C content, as shown in Figure 3d.

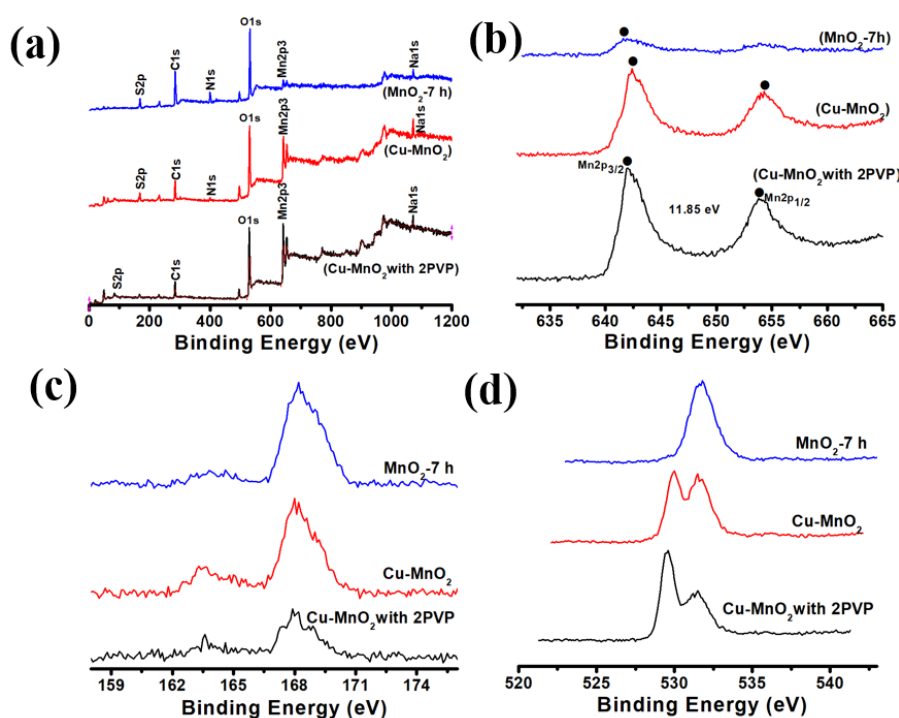


Figure 3. The XPS survey spectrum of (a) MnS-7 h, Cu-MnS, Cu-MnS with 2PVP and high resolution spectra of (b) Mn2p, (c) S2p and (d) O1s of MnS-7 h, Cu-MnS and Cu-MnS with 2PVP composite.

In this study, nickel foam was used as a substrate that exhibits good electrical conductivity and a 3D hierarchical structure with open macropores that allow prompt ion and electron transfer. Figure 4a,c presents FE-SEM images of bare MnS and Cu-MnS grown on nickel foam, and Figure 4b,d show their corresponding magnified images. The surface of MnS consists of distinct wrinkled nanotubes that can be seen from their end tips (Figure 4b), which might have emerged during the hydrothermal cooling process due to a divergence in the coefficient of thermal expansion [30]. These wrinkled nanotubes can serve as nucleation sites for the growth of Cu-MnS with PVP nanostructures as well as allow the uniform distribution of Cu and PVP. After adding 10 wt.% of Cu into MnS, the surface morphology did not change substantially but the length (580–600 nm) and diameter (100 nm) of the nanotubes decreased, which revealed the agglomeration of wrinkled nanotubes.

The effect of PVP in Cu-MnS with three different concentrations on the surface morphologies of the samples was then evaluated, as shown in Figure 5. The Cu-MnS with 1PVP nanocomposite exhibited a combination of nanomushroom and nanoflower-like structured morphologies. The low magnification SEM images covering more than 10 μm in length, displayed many nanoflower like structures, which were not uniform in morphology and formed many micro/nanogaps. High resolution images (Figure 5b) show that the flower composed of number of interlaced flakes. Figure 5a,b shows that the cross-linked flakes agglomerate together declining the available sites for electrochemical process. Compared with Cu-MnS with 1PVP, uniform and great surface adhesion on nickel foam was observed for Cu-MnS with 2PVP, which is expected have a more number of accessible charge transfer channels for redox reaction and much more effective surface due to their synergistic effect [31].

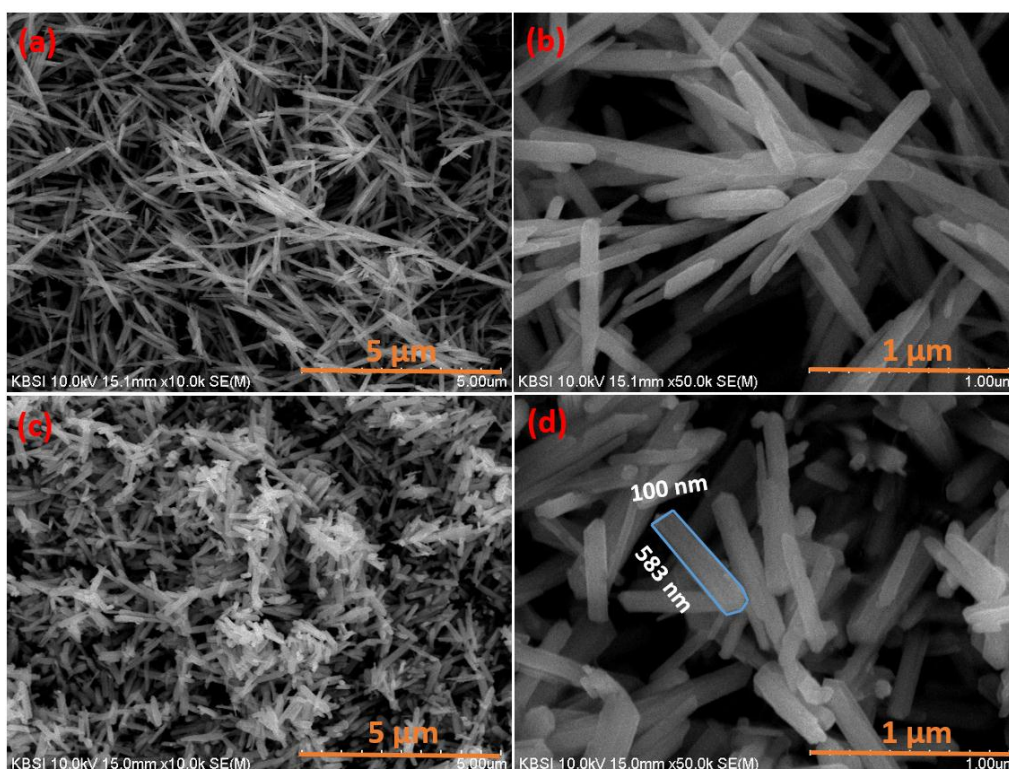


Figure 4. HR-SEM images: low magnification images of (a) MnS, (c) Cu-MnS and high-magnifications images of (b) MnS, (d) Cu-MnS.

Moreover, the 1PVP and 2PVP might have a synergistic effect and boost the electrical contact between MnS and Cu, which provides a large surface area, and might enhance the electrochemical performance. The proposed method is easier than the already published hydrothermal methods using PVP with high thermal and mechanical conductivity, which would establish the high electrical conductivity that further increases the rate performance. Interestingly, when the PVP concentration was prolonged further to 0.3 g (Figure 5f), all leaves shrank and a few degraded, which provides a crouched specific surface accessible to the aqueous electrolyte as well as enhanced electron transfer resistance compared to Cu-MnS with 1PVP and 2PVP, which should have a significant diminishing effect on the specific capacitance.

A thermogravimetric study was carried out over the temperature range of 50–800 °C; Figure S1 presents the corresponding curve (weight loss (%) versus temperature). The as-wrinkled nanotubes of MnS-7 h, containing mainly metal and sulfur precursors, degraded continuously between 100 °C to 800 °C, where a steady weight loss of 14.55% was observed, which could be due to the solvent present in the as-wrinkled nanotubes and to the evaporation of water. The agglomeration of wrinkled nanotubes (Cu-MnS) degrades via three main steps. The first weight loss of approximately 2% was observed between 100 °C to 450 °C, which might be due to the evaporation of water. A second step occurs between 450 °C to 580 °C where a steady weight loss of 20% was observed, which may be due to the decomposition of the metal precursor. The third weight loss of 2.52% until 800 °C was assigned to further decomposition of the metal precursors. Improved thermal stability was observed with respect to the pure Cu and 2PVP content in MnS up to 550 °C and a continuous weight loss was observed between 550 and 800 °C due to the decomposition of PVP.

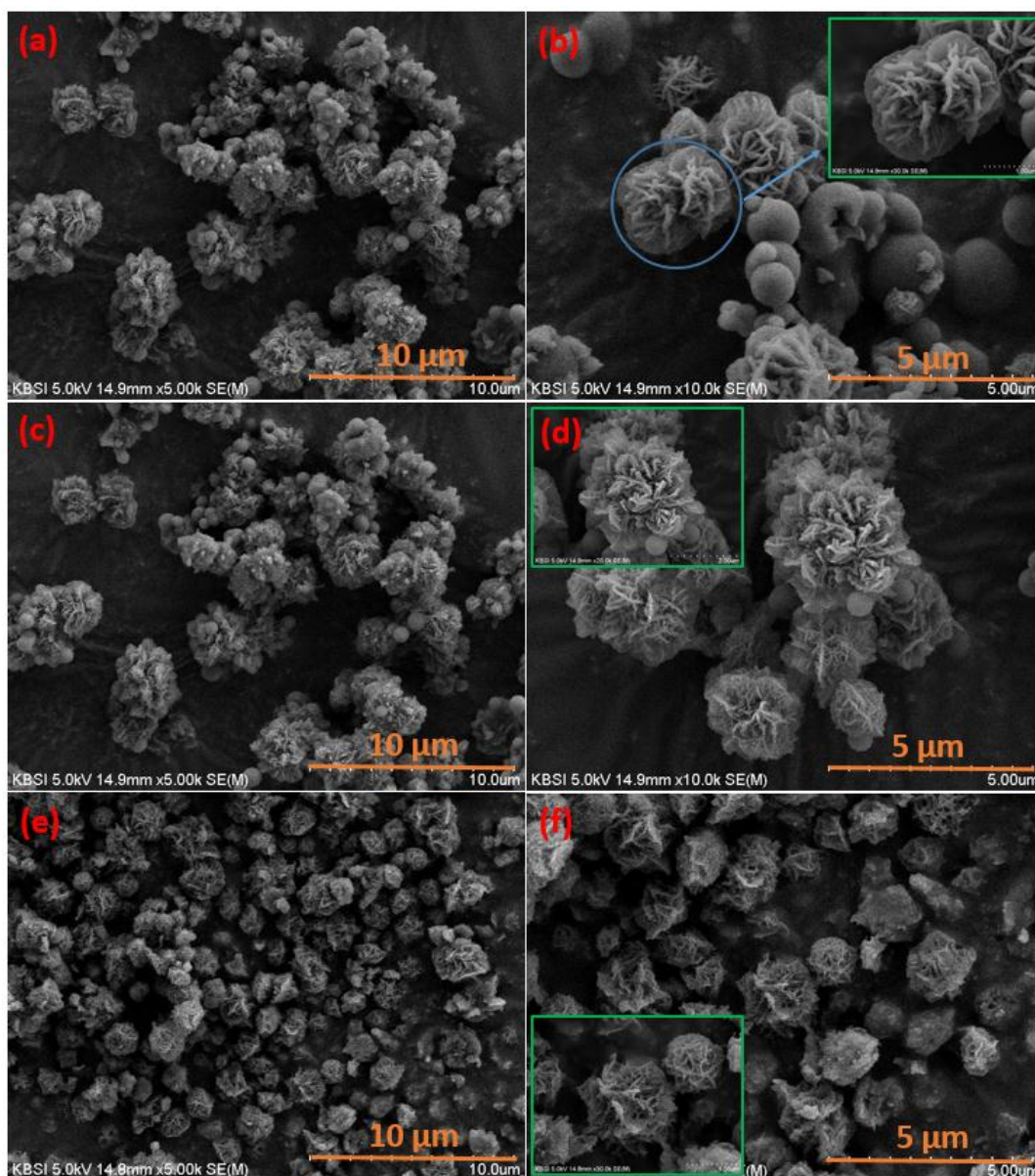


Figure 5. HR-SEM images: Cu-MnS with 1PVP, Cu-MnS with 2PVP and Cu-MnS with 3PVP (a,c,e) low magnification images and (b,d,f) high-magnifications images.

Based on the above results, all the characterizations showed that the Cu-MnS with 2PVP strongly attached to the nickel foam substrate using the brush-coated method combining a hydrothermal reaction. The assembled Cu-MnS with 2PVP electrodes displayed cabbage plant-like nanostructures with two dominances for the increase in electrochemical capacitor performance: the large surface area ameliorated from the PVP composition, which could contribute sufficient electro-active species and minimize the ion diffusion path for electrolyte ions during the electrochemical process; and high conductivity, which could affect the kinetics of electron transport [32–34].

To explore the electrochemical capacitor behavior of the as-prepared MnS, Cu-MnS, and Cu-MnS with PVP electrodes, cyclic voltammetry (CV) was performed using a three-electrode cell in 2 M KOH aqueous solution at the scan rate of 25 mV/s with a potential range from -0.5 to 0.5 V using Ag/AgCl and Pt wire as the reference and counter electrode. CV, GCD, and EIS measurements are one of the ideal tools for measuring the electrochemical performance of the electrode material for supercapacitors. As shown in Figure 6, the CV curve of the MnS electrode prepared for 7 h exhibited the largest

surface area compared to the MnS-5 and MnS-10 h-based electrodes, indicating better electrochemical performance. As reported in the literature, such a high specific capacitance was attributed to the unique 1-D nanostructure of the MnS nanorods (Figure 4a) and the charge storage mechanism of the MnS nanorods is mainly a surface process, which consists of the intercalation/de-intercalation of alkali cations. The electrochemical properties including GCD, and EIS curves for MnS-5, MnS-7, and MnS-10 h are shown in supporting information (Figure S2). The specific capacitance of MnS-7 h as a function of different current density is shown in Figure S2c. The maximum specific capacitance is as high as 154.26 F g^{-1} at 1 A g^{-1} , which is higher than that of MnS-5 and MnS-10 h based electrodes. Figure S3 shows the CV curve of the bare nickel foam at scan rate of 25 mV s^{-1} in same amount of KOH electrolyte and it can be concluded that the capacitance is much smaller than that of the MnS-5, MnS-7, and MnS-10 h based electrodes, suggesting that the current collector does not contribute to the capacitance.

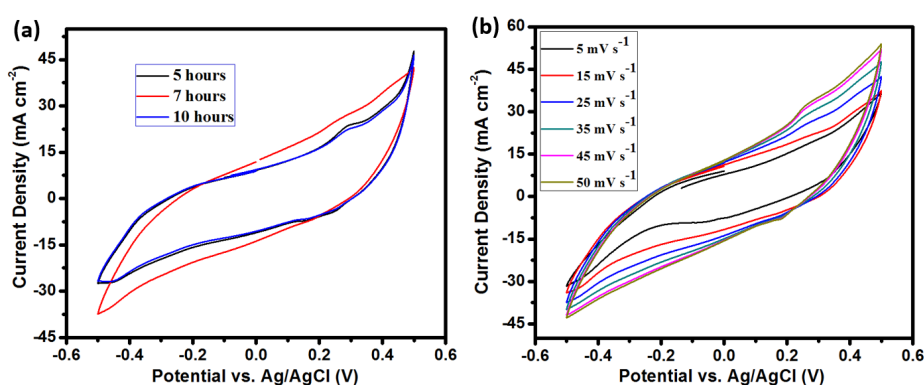


Figure 6. (a) Electrochemical performance of supercapacitors based on MnS coated on nickel foam with varying preparation times for 5, 7, and 10 h. (b) CV curves of MnS prepared for 7 h based supercapacitors for different scan rates in 2 M KOH solution.

Figure 7a,b also showed the influence of the different mass ratios of PVP in Cu-MnS on the capacitor performance. Figure 7a,b present the CV traces of Cu-MnS, Cu-MnS with the 1PVP, 2PVP, and 3PVP electrodes. All PVP-modified Cu-MnS electrodes displayed excellent pseudo-capacitor behavior. The Cu-MnS with 2PVP showed an exceptional area and higher current density values compared to the other electrodes, which indicates a rapid charge transfer rate and high capacitance at a scan rate of 5 mV s^{-1} (Figure 7b) [35]. Figure 7c shows the CV curves of the Cu-MnS with 2PVP at scan rates of 5, 15, 25, 35, 45, and 50 mV s^{-1} . These curves indicate a rapid charge transfer rate with enhanced current density. The specific capacitance (SC) decreased with increasing scan rate due to the increase in internal resistance of the electrode, produced by the crash of ionic species, which do not have sufficient time to pass electrolyte ions and electrons deep into the micropores/mesopores of the nanocomposite material [36,37]. Moreover, previous results suggested that micropores and mesopores with sizes less than $\sim 5 \text{ nm}$ have lower activity at high scan rate/current densities. As shown in Figure 7c and Figure S3 (CV curves of Cu-MnS, Cu-MnS with 1PVP and 3PVP with different scan rates), the positive and negative shifts observed at higher scan rates, which replicate the imperfect redox reaction and the loss of a few peaks, indicate partial loss of the redox reaction [38].

Figure 8a shows the GCD measurements for the resulting electrodes tested at a current density of 1 A g^{-1} in a 2 M KOH solution. The SC, and energy and power densities were calculated from the GCD curves using Equations (S3)–(S5) in supporting information. Inconsistent with the CV results, the PVP-based electrodes showed the longest discharge time and the calculated SC of Cu-MnS, Cu-MnS with 1PVP, 2PVPm, and 3PVP were 203.83, 251.8, 833.58, and 495.58 F g^{-1} at 1 A g^{-1} . The galvanostatic SC of the Cu-MnS with the 2PVP electrode material was performed at current densities ranging from 1 to 8 A g^{-1} . These curves appear to be almost symmetrical over the potential range of 0.4 to -0.5 V ,

indicating that the prepared material has greater reversibility for the charge/discharge process [39]. Therefore, the synthesized Cu-MnS with 2PVP can be considered an ultimate supercapacitor electrode material. In general, the high charge transfer rate and lower surface area of the electrode restrained ion and electron transport at the electrochemical interfaces, which led to a significant decrease in SC [36]. The introduction of copper and PVP to MnS can enhance these factors and successfully enriched the in-plane ion diffusion coefficient and SC. Importantly, the synergistic effect between Cu, PVP, and MnS helped increase the contact area between the aqueous electrolyte and electrode materials, which produced abundant electro-active sites. The highest SC of Cu-MnS with 2PVP (833.58 and 581.64 F g⁻¹ at 1 and 2 A g⁻¹) in the current case indicates the superior capacitive performance compared to the previously reported studies based on MnS and their composite. The CV curves at different scan rates, the GCD curves at different currents, and Nyquist plots of bare MnS for different deposition times (5, 7, and 10 h), Cu-MnS, and Cu-MnS with 1 and 3PVP electrodes, are shown in the supporting information (Figures S2 and S4–S6). Additionally, the GCD test was performed for bare nickel foam (Figure S7) and the discharge time is very low and it can be ignored compared with Cu-MnS with 2PVP based electrodes.

EIS further revealed the precise electrical conductivity of the electrode in the frequency region from 100 kHz to 0.01 Hz under open-circuit conditions at room temperature (Figure 8c). The Nyquist plots in Figure 6f for the Cu-MnS and Cu-MnS with the PVP-based thin film electrodes showed two distinct regions in the plot—i.e., a distorted semicircle at the high frequency region and a straight line in the low frequency region—which represents the charge transfer process and capacitive nature of the electrode, respectively. Similar high frequency intercepts were observed for the Cu-MnS and Cu-MnS with 2PVP based electrodes, indicating that they have similar ohmic resistance (the combination of contact resistance between the active materials on the Ni foam and the current collector, the intrinsic resistance of the active materials, and the ionic resistance of the aqueous electrolyte). The Cu-MnS with 2PVP composite electrode had a lower charge transfer resistance (R_{ct}), which was significantly lower than that of the Cu-MnS, 1PVP, and 3PVP-based electrodes. This suggests that the Cu and appropriate amount of PVP in MnS can decrease the R_{ct} , significantly. This shows that the low Faraday resistance contributes to the enhanced SC and power of the Cu-MnS with 2PVP composite electrode in a KOH solution [40,41].

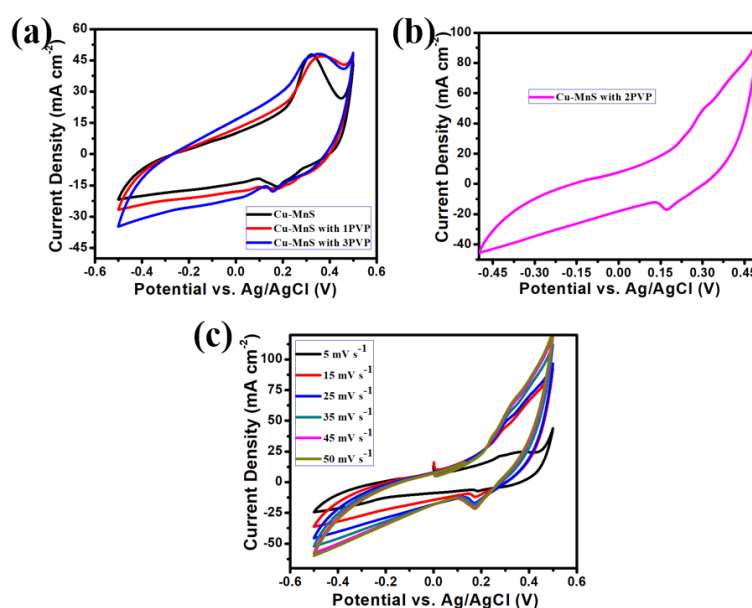


Figure 7. Cyclic voltammetry of (a) Cu-MnS, Cu-MnS with 1PVP, Cu-MnS with 3PVP and (b) Cu-MnS with 2PVP curves at scan rate of 25 mV s⁻¹. (c) CV of Cu-MnS with 2PVP electrodes at various scan rate from 5 to 50 mV s⁻¹.

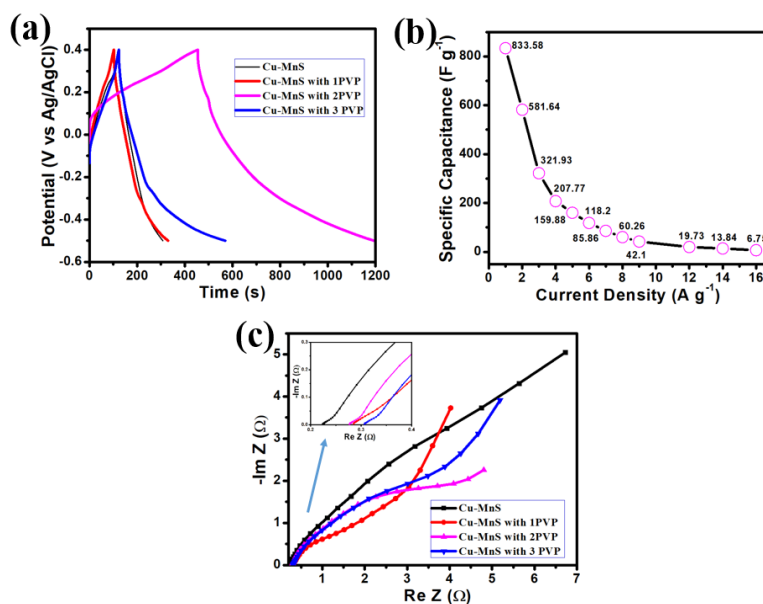


Figure 8. (a) Galvanostatic charge–discharge profile of four different electrodes at current density of 1 A g⁻¹ in 2 M KOH solution and (b) specific capacitance values calculated from the GCD curves of Cu-MnS with 2PVP electrodes as a function of current densities. (c) Nyquist profile of Cu-MnS, Cu-MnS with 1PVP, Cu-MnS with 2PVP, and Cu-MnS with 3PVP electrodes respectively.

The long-term stability of the Cu-MnS and Cu-MnS with 2PVP electrodes was also performed at a current density of 1 A g⁻¹ for 1000 cycles. Figure 9 shows that the specific capacitance decreased from 203.83 to 187.11 F g⁻¹ during stability test after 1000 cycles for Cu-MnS electrodes, implying the deactivation of electrode in KOH. While the specific capacitance of Cu-MnS with 2PVP electrode is for higher than that of Cu-MnS and only 3.05% decrement was observed, indicating excellent cycling stability. As illustrated in the Figure S8, the surface morphology was well maintained and preserved with little structural deformation after 1000 cycles. In this study, the presence of an appropriate amount of PVP in Cu-MnS is favorable for improving the electrochemical performance of the electrode and the existence of Cu was inclined to enhance the electrical conductivity. The Cu-MnS with 2PVP electrode is a good reference for researchers to design and fabricate new electrode materials with enhanced capacitive performance.

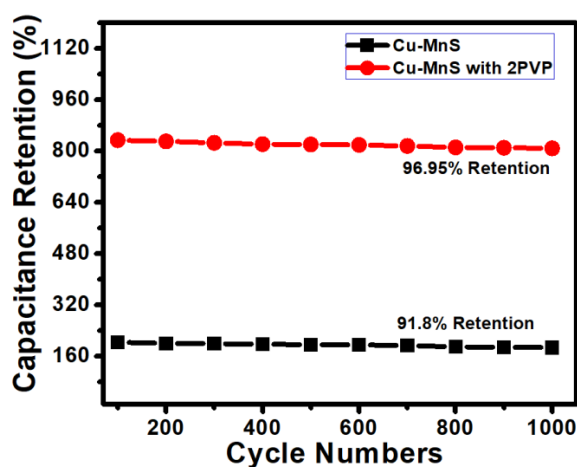


Figure 9. Capacitance retention as a function of the cycle numbers at current density of 1 A g⁻¹ in 2 M KOH solution.

4. Conclusions

In summary, cabbage plant-like nanostructured Cu-MnS with 2PVP materials were synthesized by a facile and low-cost hydrothermal approach. The Cu-MnS with 2PVP samples on Ni foam were investigated as the free-standing electrode material for electrochemical supercapacitor applications and exhibited a higher specific capacitance of 833.58 F g^{-1} at 1 A g^{-1} , good rate capability and extraordinary electrochemical cycling performance. In addition, Cu-MnS and Cu-MnS with 1 and 3 PVP produced a specific capacitance of 203.83, 251.8, and 495.58 F g^{-1} at 1 A g^{-1} . The excellent electrochemical properties were attributed mainly to the following two factors: (1) the large surface area ameliorated from the PVP composition, which could contribute sufficient electro active species and minimize the ion diffusion path for electrolyte ions during the electrochemical process, electron transfer, and better accommodation to the volume change during long-term charge–discharge process; and (2) its high conductivity and surface area, which could affect the electron transport kinetics. These results suggest that the electrode material is a good candidate for high energy and power density applications that are practical for large scale use.

Supplementary Materials: The following are available online at <http://www.mdpi.com/1996-1073/11/6/1590/s1>, Figure S1. Thermogravimetric images of as-prepared MnS, Cu-MnS and Cu-MnS with 2PVP samples. Figure S2. (a) Galvanostatic charge–discharge curves of supercapacitors using MnS material with different preparation time. (b) GCD curves of MnS-7 h at different current densities. (c) Specific capacitance calculated from the GCD curves of MnS-7 h as a function of current densities. (d) Nyquist curves in 2 M KOH solution at frequency range from 100 kHz to 0.1 Hz. Figure S3. CV curve of bare nickel foam in KOH electrolyte at scan rate of 25 mV s^{-1} . Figure S4. Cyclic voltammetry of (a) Cu-MnS, (b) Cu-MnS with 1PVP, and (c) Cu-MnS with 3PVP with different scan rates in 2 M KOH solution. Figure S5. (a) Galvanostatic charge–discharge curves of Cu-MnS at different current densities in 2 M KOH solution. (b) Specific capacitance of Cu-MnS electrode calculated from the GCD curves as a function of current densities. Figure S6. (a) Galvanostatic charge–discharge curves of Cu-MnS with 1PVP at different current densities in 2 M KOH solution. (b) Specific capacitance of Cu-MnS electrode calculated from the GCD curves as a function of current densities. Figure S7. GCD curve of bare nickel foam in KOH electrolyte. Figure S8. HR-SEM image of Cu-MnS with 2PVP after stability test.

Author Contributions: S.S.R wrote the manuscript and carried out experiment with support from J.-W.A. and I.K.D. J.-W.A. helped during revision time with S.S.R. B.N and B.J.-S developed the theory and helped during experiment section. T.N.V.K and C.I.-H verified the experimental results. H.-J.K. investigate and supervised the funding of this work.

Funding: This research received no external funding.

Acknowledgments: This work was supported by BK 21 PLUS, Creative Human Resource Development Program for IT Convergence, Pusan National University, Busan, South Korea for its financial support. In addition, this work was supported by the Human Resources Program in Energy Technology of the Korea Institute of Energy Technology Evaluation and Planning (KETEP) granted financial resource from the Ministry of Trade, Industry & Energy, Republic of Korea. (no. 20164010200940). Finally, thanks to the KBSI for the instrumental characterizations.

Conflicts of Interest: The authors declare no conflict of interest.

References

1. Rao, S.S.; Punnoose, D.; Bae, J.H.; Durga, I.K.; Varma, C.V.T.; Naresh, B.; Subramanian, A.; Raman, V.; Kim, H.J. Preparation and electrochemical performances of NiS with PEDOT:PSS chrysanthemum petal like nanostructure for high performance supercapacitors. *Electrochim. Acta* **2017**, *254*, 269–279.
2. Rao, S.S.; Durga, I.K.; Kundakarla, N.; Punnoose, D.; Gopi, C.V.V.M.; Reddy, A.E.; Jagadeesh, M.; Kim, H.J. A hydrothermal reaction combined with a post anion-exchange reaction of hierarchically nanostructured NiCo_2S_4 for high-performance QDSSCs and supercapacitors. *New J. Chem.* **2017**, *41*, 10037–10047. [[CrossRef](#)]
3. Xiang, D.; Bote, Z.; Liang, Z.; Zongping, S. Molten salt synthesis of nitrogen-doped carbon with hierarchical pore structures for use as high-performance electrodes in supercapacitors. *Carbon* **2015**, *93*, 48–58.
4. Bote, Z.; Lei, Z.; Qiaobao, Z.; Dongchang, C.; Yong, C.; Xiang, D.; Yu, C.; Ryan, M.; Xunhui, X.; Bo, S.; et al. Rational design of nickel hydroxide-based nanocrystals on graphene for ultrafast energy storage. *Adv. Energy Mater.* **2018**, *8*, 1702247.

5. Shuge, D.; Bote, Z.; Chong, Q.; Dongchang, C.; Dai, D.; Bo, S.; Ben, M.D.; Jianwei, F.; Chenguo, H.; Ching-Ping, W.; et al. Controlled synthesis of three-phase $\text{Ni}_x\text{S}_y/\text{rGO}$ nanoflake electrodes for hybrid supercapacitors with high energy and power density. *Nano Energy* **2017**, *33*, 522–531.
6. Bote, Z.; Dongchang, C.; Xunhui, X.; Bo, S.; Renzong, H.; Qiaobao, Z.; Benjamin, H.R.; Gordon, H.W.; Dongxing, Z.; Yong, D.; et al. A high-energy, long cycle-life hybrid supercapacitor based on graphene composite electrodes. *Energy Storage Mater.* **2017**, *7*, 32–39.
7. Gao, R.; Zhang, Q.; Soyekwo, F.; Lin, C.; Lv, R.; Qu, Y.; Chen, M.; Zhu, A.; Liu, Q. Novel amorphous nickel sulfide@CoS double-shelled polyhedral nanocages for supercapacitor electrode materials with superior electrochemical properties. *Electrochim. Acta* **2017**, *237*, 94–101. [[CrossRef](#)]
8. Huang, L.; Hou, H.; Liu, B.; Zeinu, K.; Yuan, X.; Zhu, X.; He, X.; Wu, L.; Hu, J.; Yang, J. Phase-controlled solvothermal synthesis and morphology evolution of nickel sulfide and its pseudocapacitance performance. *Ceram. Int.* **2017**, *43*, 3080–3088. [[CrossRef](#)]
9. Song, X.; Tan, L.; Wang, X.; Zhu, L.; Yi, X.; Dong, Q. Synthesis of CoS@rGO composites with excellent electrochemical performance for supercapacitors. *J. Electroanal. Chem.* **2017**, *794*, 132–138. [[CrossRef](#)]
10. Subramani, K.; Sudhan, N.; Divya, R.; Sathish, M. All-solid-state asymmetric supercapacitors based on cobalt hexacyanoferrate-derived CoS and activated carbon. *RSC Adv.* **2017**, *7*, 6648–6659. [[CrossRef](#)]
11. Adnan, Y.; Dewei, C.; Sean, L. Ethanol-directed morphological evolution of hierarchical CeOx architectures as advanced electrochemical capacitors. *J. Mater. Chem. A* **2015**, *3*, 13970–13977.
12. Zhu, G.; He, Z.; Chen, J.; Zhao, J.; Feng, X.; Ma, Y.; Fan, Q.; Wang, L.; Huang, W. Highly conductive three-dimensional MnO_2 -carbon nanotube-graphene-Ni hybrid foam as a binder-free supercapacitor electrode. *Nanoscale* **2014**, *6*, 1079–1085. [[CrossRef](#)] [[PubMed](#)]
13. Wu, D.; Xu, S.; Zhang, C.; Zhu, Y.; Xiong, D.; Huang, R.; Qi, R.; Wang, L.; Chu, P.K. Three-dimensional homo-nanostructured MnO_2 /nanographene membranes on a macroporous electrically conductive network for high performance supercapacitors. *J. Mater. Chem. A* **2016**, *4*, 11317–11329. [[CrossRef](#)]
14. Chhowalla, M.; Shin, H.S.; Eda, G.; Li, L.J.; Loh, K.P.; Zhang, H. The chemistry of two-dimensional layered transition metal dichalcogenide nanosheets. *Nat. Chem.* **2013**, *5*, 263–275. [[CrossRef](#)] [[PubMed](#)]
15. Sahoo, S.; Mondal, R.; Late, D.J.; Rout, C.S. Electrodeposited Nickel Cobalt Manganese based mixed sulfide nanosheets for high performance supercapacitor application. *Microporous Mesoporous Mater.* **2017**, *244*, 101–108. [[CrossRef](#)]
16. Rao, S.S.; Durga, I.K.; Gopi, C.V.V.M.; Tulasivarma, C.V.; Kim, S.K.; Kim, H.J. The effect of TiO_2 nanoflowers as a compact layer for CdS quantum-dot sensitized solar cells with improved performance. *Dalton Trans.* **2015**, *44*, 12852–12862. [[CrossRef](#)] [[PubMed](#)]
17. Rao, S.S.; Gopi, C.V.V.M.; Kim, S.K.; Son, M.K.; Jeong, M.S.; Savariraj, A.D.; Prabakar, K.; Kim, H.J. Cobalt sulfide thin film as an efficient counter electrode for dye-sensitized solar cells. *Electrochim. Acta* **2014**, *133*, 174–179.
18. Cheng, J.; Yan, H.; Lu, Y.; Qiu, K.; Hou, X.; Xu, J.; Han, L.; Liu, X.; Kim, J.K.; Luo, Y. Mesoporous CuCo_2O_4 nanograsses as multi-functional electrodes for supercapacitors and electro-catalysts. *J. Mater. Chem. A* **2015**, *3*, 9769–9776. [[CrossRef](#)]
19. Pang, H.; Wang, S.; Li, G.; Ma, Y.; Li, J.; Li, X.; Zhang, L.; Zhang, J.; Zheng, H. Cu superstructures fabricated using tree leaves and Cu-MnO₂ superstructures for high performance supercapacitors. *J. Mater. Chem. A* **2013**, *1*, 5053–5060. [[CrossRef](#)]
20. Cai, M.; Qian, H.; Wei, Z.; Chen, J.; Zheng, M.; Dong, Q. Polyvinyl pyrrolidone-assisted synthesis of a Fe_3O_4 /graphene composite with excellent lithium storage properties. *RSC Adv.* **2014**, *4*, 6379–6382. [[CrossRef](#)]
21. Zhang, X.; Wang, J.; Jia, H.; Yin, B.; Ding, L.; Xu, Z.; Ji, Q. Polyvinyl pyrrolidone modified graphene oxide for improving the mechanical, thermal conductivity and solvent resistance properties of natural rubber. *RSC Adv.* **2016**, *6*, 54668–54678. [[CrossRef](#)]
22. Joshi, K.V.; Joshi, B.K.; Harikrishna, U.; Patel, M.B.; Menon, S.K. Polyvinyl pyrrolidone modified ZnS nanoparticles as a highly selective and sensitive nanosensor for the iodide ion. *Anal. Methods* **2013**, *5*, 4973–4977. [[CrossRef](#)]
23. Yang, G.W.; Xu, C.L.; Li, H.L. Electrodeposited nickel hydroxide on nickel foam with ultrahigh capacitance. *Chem. Commun.* **2008**, *48*, 6537–6579. [[CrossRef](#)] [[PubMed](#)]

24. Lu, M.; Yuan, X.P.; Guan, X.H.; Wang, G.S. Synthesis of nickel chalcogenide hollow spheres using an L-cysteine-assisted hydrothermal process for efficient supercapacitor electrodes. *J. Mater. Chem. A* **2017**, *5*, 3621–3627. [[CrossRef](#)]
25. Xia, Q.; Xu, M.; Xia, H.; Xie, J. Nanostructured Iron Oxide/Hydroxide-based electrode materials for supercapacitors. *ChemNanoMat* **2016**, *2*, 588–600. [[CrossRef](#)]
26. Liu, R.M.; Jian, Z.X.; Liu, Q.; Zhu, X.D.; Liu, L.; Ni, L.; Shen, C.C. Novel red blood cell shaped α -Fe₂O₃ microstructures and FeO(OH) nanorods as high capacity supercapacitors. *RSC Adv.* **2015**, *5*, 91127–91133. [[CrossRef](#)]
27. Kim, H.J.; Kim, C.W.; Punnoose, D.; Gopi, C.V.V.M.; Kim, S.K.; Prabakar, K.; Rao, S.S. Nickel doped cobalt sulfide as a high performance counter electrode for dye-sensitized solar cells. *Appl. Surf. Sci.* **2015**, *328*, 78–85. [[CrossRef](#)]
28. Ummartyotin, S.; Bunnak, N.; Juntaro, J.; Sain, M.; Manuspiya, H. Synthesis and luminescence properties of ZnS and metal (Mn, Cu)-doped-ZnS ceramic powder. *Solid State Sci.* **2012**, *14*, 299–304. [[CrossRef](#)]
29. Ramachandran, R.; Saranya, M.; Grace, A.N.; Wang, F. MnS nanocomposites based on doped graphene: Simple synthesis by a wet chemical route and improved electrochemical properties as an electrode material for supercapacitors. *RSC Adv.* **2017**, *7*, 2249–2257. [[CrossRef](#)]
30. Anothumakkool, B.; Torris, A.T.A.; Bhange, S.N.; Badiger, M.V.; Kurungot, S. Electrodeposited polyethylenedioxythiophene with infiltrated gel electrolyte interface: A close contest of an all-solid-state supercapacitor with its liquid-state counterpart. *Nanoscale* **2014**, *6*, 5944–5952. [[CrossRef](#)] [[PubMed](#)]
31. Zhiguo, Z.; Xiao, H.; Huan, L.; Hongxia, W.; Yingyuan, Z.; Tingli, M. All-solid-state flexible asymmetric supercapacitors with high energy and power densities based on NiCo₂S₄@MnS and active carbon. *J. Energy Chem.* **2017**, *26*, 1260–1266.
32. Moon, I.K.; Lee, J.; Ruoff, R.S.; Lee, H. Reduced graphene oxide by chemical graphitization. *Nat. Commun.* **2010**, *1*, 73. [[CrossRef](#)] [[PubMed](#)]
33. Choi, B.G.; Hong, J.; Hong, W.H.; Hammond, P.T.; Park, H. Facilitated ion transport in all-solid flexible supercapacitors. *ACS Nano* **2011**, *5*, 7205–7213. [[CrossRef](#)] [[PubMed](#)]
34. Lv, T.; Yao, Y.; Li, N.; Chen, T. Highly Stretchable supercapacitors based on aligned carbon nanotube/molybdenum disulfide composites. *Angew. Chem. Int. Ed.* **2016**, *55*, 9191–9195. [[CrossRef](#)] [[PubMed](#)]
35. Yang, X.; Zhao, L.; Lian, J. Arrays of hierarchical nickel sulfides/MoS₂ nanosheets supported on carbon nanotubes backbone as advanced anode materials for asymmetric supercapacitor. *J. Power Sources* **2017**, *343*, 373–386. [[CrossRef](#)]
36. Kumar, A.; Sager, A.; Kumar, A.; Mishra, Y.K.; Chandra, R. Performance of high energy density symmetric supercapacitor based on sputtered MnO₂ nanorods. *ChemistrySelect* **2016**, *1*, 3885–3891. [[CrossRef](#)]
37. Xia, H.; Zhu, D.; Luo, Z.; Yu, Y.; Shi, X.; Yuan, G.; Xie, J. Hierarchically structured Co₃O₄@Pt/MnO₂ nanowire arrays for high-performance supercapacitors. *Sci. Rep.* **2013**, *3*, 2978. [[CrossRef](#)] [[PubMed](#)]
38. Radhamani, A.V.; Shareef, K.M.; Rao, M.S.R. ZnO@MnO₂ Core-Shell nanofiber cathodes for high performance asymmetric supercapacitors. *ACS Appl. Mater. Interfaces* **2016**, *8*, 30531–30542. [[CrossRef](#)] [[PubMed](#)]
39. Cheng, T.; Zhang, Y.Z.; Yi, J.P.; Yang, L.; Zhang, J.D.; Lai, W.Y.; Huang, W. Inkjet-printed flexible, transparent and aesthetic energy storage devices based on PEDOT:PSS/Ag grid electrodes. *J. Mater. Chem. A* **2016**, *4*, 13754–13763. [[CrossRef](#)]
40. Li, W.; Wang, S.; Xin, L.; Wu, M.; Lou, X. Single-crystal β -NiS nanorod arrays with a hollowstructured Ni₃S₂ framework for supercapacitor applications. *J. Mater. Chem. A* **2016**, *4*, 7700–7709. [[CrossRef](#)]
41. Zhu, T.; Wang, Z.; Ding, S.; Chen, J.S.; Lou, X.W. Hierarchical nickel sulfide hollow spheres for high performance supercapacitors. *RSC Adv.* **2011**, *1*, 397–400. [[CrossRef](#)]

